Lattice Instability during Solid-Solid Structural Transformations under a General Applied Stress Tensor: Example of Si I → Si II with Metallization

Nikolai A. Zarkevich,[1,*] Hao Chen,[2,†] Valery I. Levitas,[1,2,3,4,‡] and Duane D. Johnson[1,4,§]
[1]*Ames Laboratory, U.S. Department of Energy, Iowa State University, Ames, Iowa 50011-3020, USA*
[2]*Department of Aerospace Engineering, Iowa State University, Ames, Iowa 50011, USA*
[3]*Department of Mechanical Engineering, Iowa State University, Ames, Iowa 50011, USA*
[4]*Department of Materials Science and Engineering, Iowa State University, Ames, Iowa 50011, USA*

(Received 2 June 2018; published 17 October 2018)

The density functional theory was employed to study the stress-strain behavior and elastic instabilities during the solid-solid phase transformation (PT) when subjected to a general stress tensor, as exemplified for semiconducting Si I and metallic Si II, where metallization precedes the PT, so stressed Si I can be a metal. The hydrostatic PT occurs at 76 GPa, while under uniaxial loading it is 11 GPa (3.7 GPa mean pressure), 21 times lower. The Si I → Si II PT is described by a critical value of the phase-field's modified transformation work, and the PT criterion has only two parameters given six independent stress elements. Our findings reveal novel, more practical synthesis routes for new or known high-pressure phases under predictable nonhydrostatic loading, where competition of instabilities can serve for phase selection rather than free energy minima used for equilibrium processing.

DOI: 10.1103/PhysRevLett.121.165701

Phase transformations (PTs) in solids are mostly characterized by equilibrium phase diagrams [1], whereas general nonhydrostatic stresses offer novel synthetic routes for new or known high-pressure phases. Here we augment temperature-pressure ($T-P$) equilibrium diagrams by a stress ($\boldsymbol{\sigma}$) tensor that affects structural (and electronic) instabilities, providing guidance for creating more accessible processing routes of such phases under predictable nonhydrostatic deformation at significantly lower mean pressures. Indeed, observed PTs occur under a significant deviation from equilibrium [2–5], with large hysteresis. For carbon, the graphite-diamond PT at room temperature occurs at 2.45 GPa; however, due to hysteresis, the PT is observed at 70 GPa [3]. The actual PT pressure deviates from that of equilibrium due to an enthalpy barrier. When thermal fluctuations can be neglected, the PT criterion is related to disappearance of the enthalpy barrier, i.e., to the lattice instability. Hence, lattice instability conditions are necessarily studied under hydrostatic, uniaxial, and multiaxial loadings [6–12].

In experiments, a significant reduction in PT pressure occurs due to deviatoric (nonhydrostatic) stresses and plastic strains [5,13–16]. For example, plastic shear reduces the PT from hexagonal to superhard wurtzitic BN from 52.8 to 6.7 GPa [5]—an order of magnitude. This phenomenon is extremely important from fundamental and applied points of view, as it may reduce the PT pressure to a practical level for high-pressure phases that exhibit unique properties.

The suggested physical mechanism responsible for this reduction is related to dislocation pileups associated with a plastic strain [13]. As stresses at the tip of a pileup are proportional to the number of dislocations in a pileup (typically 10–100), local stresses exceed the lattice instability limit and cause the nucleation of a high-pressure phase even at a relatively small external pressure. This was rationalized based on an analytical model [13] and using a phase-field approach [17,18]. However, the phase-field inputs for the PT instability criteria for an ideal crystal under a *general stress tensor* were assumed hypothetically, as such criteria are not known for any material [19].

Because of the technological importance of Si and its PTs, a huge literature exists. Relevant are the PTs in Si I under hydrostatic and two-parametric nonhydrostatic loadings, studied with the density functional theory (DFT) [20,21], and the lattice instability under two-parametric loadings (unrelated to a PT) [10,22–24].

So, we perform a DFT study of the deformation process under an applied *general stress* and determine the lattice instabilities responsible for the cubic-to-tetragonal Si I → Si II PT, along with metallization that can occur prior to the Si II phase. While finding the instability criteria under all six stress components seems daunting, due to the large number of combinations, unexpected guidance came from the crystal lattice instability criterion formulated within the phase-field method [11,12,25,26]. The key result is that Si I → Si II PT can be described by the critical value of the modified transformation work. With normal stresses (σ_1, σ_2, σ_3) acting along $\langle 110\rangle$, $\langle 1\bar{1}0\rangle$, and $\langle 001\rangle$, respectively, the PT criterion is linear in normal stresses, depends on $\sigma_1+\sigma_2$, is independent of $\sigma_1-\sigma_2$ and shear stress τ_{21}, acting alone or with one more shear stress, and depends on

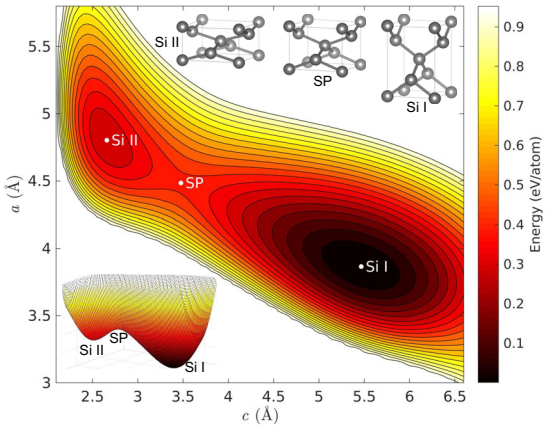

FIG. 1. DFT energy of Si versus lattice parameters c and a. Insets: Tetragonal ($a = b$, c) unit cells for stress-free Si II (left), unstable SP (middle), and Si I (right).

all shear stresses via theoretically predicted geometric nonlinearity. The PT criterion has only two material parameters for a general applied stress, which can be determined by two DFT simulations under different normal stresses.

Energy landscape.—The DFT potential energy (versus lattice constants $a_i = b_i$ and c_i) is given in Fig. 1; the data are in Supplemental Material [27]. We find two local energy minima, corresponding to the fully relaxed (stress-free) Si I and Si II, and a saddle point (SP)—the unstable state corresponding to the enthalpy barrier (Fig. 1). The tetragonal cell of Si I is bounded by (110), $(1\bar{1}0)$, and (001) planes. The DFT energies and lattice constants relative to the stress-free Si I ($a_1 = 3.8653$ Å, $c_1 = \sqrt{2}a_1 = 5.4665$ Å) are 0.2949 eV/atom for Si II ($a_2 = 4.8030$ Å, $c_2 = 2.6592$ Å) and 0.4192 eV/atom for the SP state ($a = 4.4847$ Å, $c = 3.4763$ Å). The calculated c_1 is +0.7% of the experiment (5.43 Å) [40].

We designate tensors with boldface; e.g., $\boldsymbol{I}$ is the unit tensor. Contractions of tensors $\boldsymbol{A} = \{A_{ij}\}$ and $\boldsymbol{B} = \{B_{jk}\}$ over one and two indices in Einstein notations are $\boldsymbol{A}\cdot\boldsymbol{B} = \{A_{ij}B_{jk}\}$ and $\boldsymbol{A}:\boldsymbol{B} = A_{ij}B_{ji}$, respectively. The inverse and transpose of $\boldsymbol{A}$ are $\boldsymbol{A}^{-1}$ and $\boldsymbol{A}^T$, respectively.

Deformation gradient.—$\boldsymbol{F} = \boldsymbol{F}_e\cdot\boldsymbol{U}_t$, mapping an undeformed state of a crystal into a deformed state, is decomposed into elastic $\boldsymbol{F}_e$ and transformational $\boldsymbol{U}_t$ parts. Deformation gradient $\boldsymbol{U}_t$ changes the Si I stress-free cell to the Si II stress-free cell; its diagonal components are $U_{t1} = U_{t2} = a_2/a_1 = 1.243$ and $U_{t3} = c_2/c_1 = 0.486$. For a Tersoff potential [11,12], it is quite different: $U_{t1} = U_{t2} = 1.175$ and $U_{t3} = 0.553$. We label tetragonal directions $a = b$ and c by indices 1, 2, and 3. We use true Cauchy stress $\boldsymbol{\sigma}$ (force per unit deformed area) and Lagrangian strain $\boldsymbol{E} = \frac{1}{2}(\boldsymbol{F}^T\cdot\boldsymbol{F} - \boldsymbol{I})$.

Stress strain.—σ_3–E_3 curves for fixed lateral stresses $\sigma_1 = \sigma_2$ are in Fig. 2, along with corresponding transformation

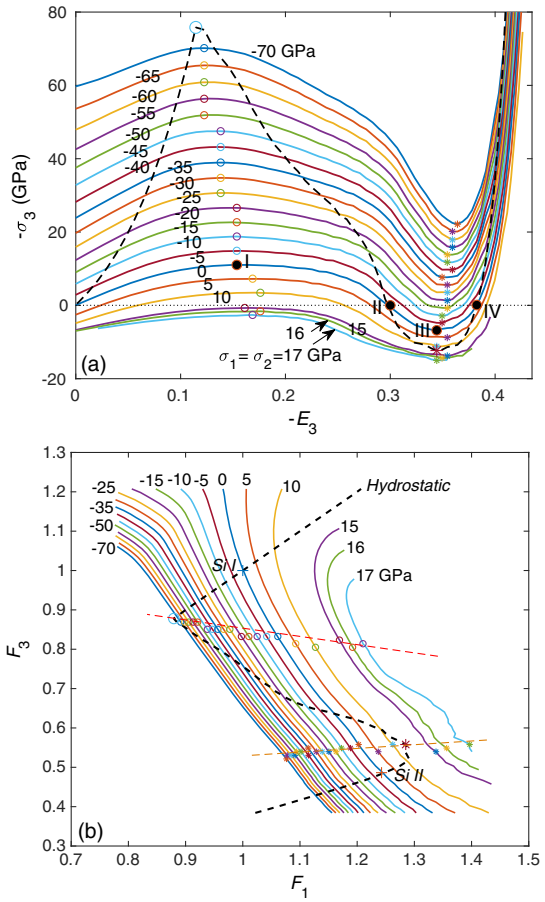

FIG. 2. (a) True (Cauchy) stress σ_3 versus Lagrangian strain E_3 for compression or tension along c for lateral stresses $\sigma_1 = \sigma_2$ for Si I ↔ Si II PTs; (b) corresponding transformation paths in the ($F_1 = F_2$, F_3) plane. Hollow (solid) symbols mark instability points for forward (reverse) PT. The dashed line shows hydrostatic loading.

paths in the ($F_1 = F_2$, F_3) plane. The elastic instability occurs when the determinant of the elastic moduli tensor, modified by some geometrically nonlinear terms, reduces to zero [6–10]. This results in a condition that some elastic moduli (or combination thereof) reduce to zero. We will use an alternative (more strict) condition: Elastic lattice instability at true stress $\boldsymbol{\sigma}$ occurs at stresses above (or below for the reverse PT) which the crystal cannot be at equilibrium. Instability points correspond to the stress maximum for forward PT (and minimum for reverse PT) on the stress-strain curves (Fig. 2). Our condition is more general and universal, because it is applicable even to the cases with discontinuous or undefined derivatives of stress with respect to strain.

A tetragonal stressed lattice of Si I transforms into a tetragonal stressed lattice of Si II (Figs. 1 and 2), and the lattice instability does not change this tetragonal symmetry. The slope of the stress-strain curve is continuous and is zero at instability points. Under hydrostatic loading (dashed line in Fig. 2), a cubic lattice loses its stability under tetragonal

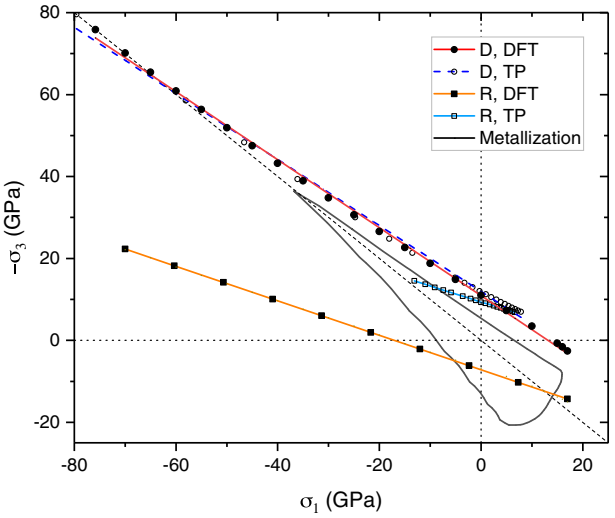

FIG. 3. Elastic instability versus σ_3 and $\sigma_1 = \sigma_2$ for direct (D) Si I → Si II and reverse (R) Si II → Si I PTs from DFT and TP-based results [11,12] and the metallization curve from DFT. Hydrostatic condition ($\sigma_1 = \sigma_2 = \sigma_3$) is a diagonal (dashed black) line.

perturbations; i.e., there is a bifurcation from a primary isotropic deformation to a secondary tetragonal deformation; hence, the derivative at the hydrostatic instability point is discontinuous. Under both hydrostatic ($\sigma_1 = \sigma_2 = \sigma_3$) and uniaxial ($\sigma_1 = \sigma_2 = 0$) compression, there are three stress-free states (Fig. 1): Si I, Si II (stable or metastable enthalpy minima), and an intermediate unstable state at the SP (enthalpy barrier). Interestingly, a stress-free Si II is metastable with stable phonons [21,41,42]. Thus, one could search for a pressure-plastic shear path for arresting the metastable Si II, as suggested in Ref. [13] for any metastable phase. In experiments, a stress-free Si II was not observed.

Elastic lattice instability.—conditions under two-parametric loading at $\sigma_1 = \sigma_2$ for forward (direct) (σ_{3d}) and reverse (σ_{3r}) PTs are approximated by linear relationships in Fig. 3. Tersoff-potential (TP) results from Refs. [11,12] for Si I → Si II PT are generally in good agreement with the present DFT results; however, there is a difference for tensile and small compressive σ_1, where TP results are slightly higher and nonlinear. Under hydrostatic loading, the PT pressure from DFT and TP is 75.81 and 79.58 GPa, respectively.

The PT stress for uniaxial compression is −11.03 GPa (σ_{3d}) at $E_3 = -0.154$. Then the pressure for uniaxial loading is $-\sigma_{3d}/3 = 3.68$ GPa, which is $75.81/3.68 = 20.6$ times lower than the hydrostatic case. This characterizes the very strong effect of nonhydrostatic stresses on PT, which can partially explain a scatter in experimental data under quasihydrostatic conditions and a significantly lower experimental PT pressure than the predicted hydrostatic instability pressure. The instability lines are described by $\sigma_{3d} = -10.9 + 1.20\sigma_1$ for $\sigma_1 \subset [-75.81; 17]$ and $\sigma_{3r} = 7.175 + 0.4209\sigma_1$ for $\sigma_1 \subset [-70; 17]$. The theoretical strength is approximately $\sigma_{3d} = -10.6 + 0.77\sigma_1$ for $\sigma_1 \subset [-15; 12]$. As it is close to our result, the instability in Ref. [23] is related to Si I → Si II PT.

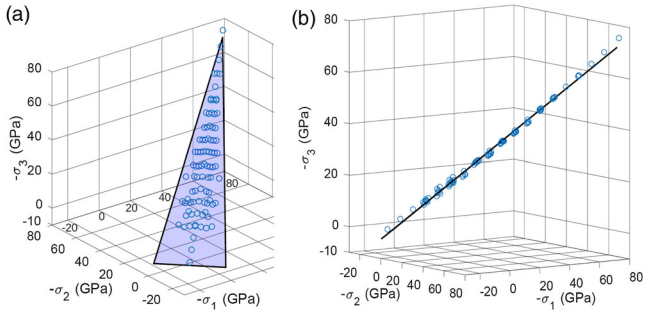

FIG. 4. Criterion for Si I → Si II PT for triaxial stresses. (a) DFT results (points) lie very close to a plane described by a constant value of modified transformation work in Eq. (3). (b) The result in (a) rotated to visualize an approximate plane.

While the instability line for forward PT, calculated in Refs. [11,12] using TP, is quite close to our DFT results, for reverse PT the TP results are completely different from DFT. Thus, none of the classical potentials in Refs. [11,12] (Tersoff, modified Tersoff, and Stillinger-Weber) are able to describe the reverse PT.

Metallization.—This electronic transition from a semiconducting to a metallic phase (band gap → zero) is caused by deformation of Si I under combinations of σ_3 and fixed $\sigma_1 = \sigma_2$ (Fig. 3). The band gap versus compressive or tensile strain is given in Fig. S2 [27]. The electronic transition is found to precede the structural PT for all combinations of stresses; i.e., a sufficiently deformed Si I under stress is metallic (Fig. 3). This transition does not change the continuity of the stress-strain curves and their first derivatives (Fig. 2); this differs from the stress discontinuity in magnetostructural phase transitions [43]. The metallization curve is closed in the (σ_3, σ_1) plane and surrounds the stress-free Si I; it can be approximated by two straight lines $\sigma_{3m} = -5.605 + 0.8417\sigma_1$ and $\sigma_{3m} = 13.04 + 1.396\sigma_1$ and a parabolic section $\sigma_{3m} = 11.95 + 2.378\sigma_1 + 0.16\sigma_1^2$. While one of the metallization lines is relatively close and approximately parallel to the Si I → Si II PT line, two other lines are deeply in the region of stability of Si I (Fig. 3). Metallization occurs at compressive −36.82 GPa and tensile +13.91 GPa under hydrostatic pressure, −5.4 and +12.78 GPa under uniaxial loading at $\sigma_1 = \sigma_2 = 0$ and −6.69 and +8.79 GPa under biaxial loading at $\sigma_3 = 0$. Hence, the effect of nonhydrostatic stresses is extremely strong.

Elastic lattice instability under triaxial loading.—Evidently, DFT results for $\sigma_1 \neq \sigma_2$ case (Fig. 4) suggest that the criterion for forward Si I → Si II PT is described accurately in 3D space of normal stresses by a plane:

$$\sigma_3 = -9.911 + 0.4145(\sigma_1 + \sigma_2). \quad (1)$$

It is very surprising that the elastic instability for a material with strong physical and geometric nonlinearities can be approximated by a linear criterion.

Lattice instability under general stress tensor—The phase-field approach.—As shown in Refs. [11,12,25,26], a PT condition linear in normal stress can be derived by the phase-field approach to martensitic PTs. Using several assumptions, the instability Si I → Si II PT criterion is

$$2W = \boldsymbol{\sigma}:\boldsymbol{F}_e^{T-1}\cdot\left.\frac{d^2\bar{\boldsymbol{U}}_t}{d\eta^2}\right|_{\eta=0}\cdot\boldsymbol{F}_e^{T} \geq 2A, \tag{2}$$

where deformation gradient $\bar{\boldsymbol{U}}_t(\eta) \equiv \boldsymbol{I} + \bar{\boldsymbol{\varepsilon}}_t(\eta)$, and other material parameters [e.g., elastic moduli and transformation strain $\bar{\boldsymbol{\varepsilon}}_t(\eta)$] depend on the order parameter η, which changes during the transformation process from $\eta = 0$ for Si I [$\bar{\boldsymbol{\varepsilon}}_t(0) = \boldsymbol{0}$] to $\eta = 1$ for Si II [$\bar{\boldsymbol{\varepsilon}}_t(1) = \boldsymbol{\varepsilon}_t = \mathrm{diag}(\varepsilon_{t1}, \varepsilon_{t1}, \varepsilon_{t3})$]. W is called the modified transformation work [11], and A is the magnitude of the double-well barrier. For a cubic-to-tetragonal transformation, $[(d^2\bar{\boldsymbol{U}}_t)/(d\eta^2)]|_{\eta=0} = 2\mathrm{diag}(b_1\varepsilon_{t1}, b_1\varepsilon_{t1}, b_3\varepsilon_{t3})$, where b_i are the coefficients in the interpolation of $\bar{\boldsymbol{\varepsilon}}_t(\eta)$. For the loading by three stresses normal to the chosen above faces, all tensors in Eq. (2) are coaxial, tensors $\boldsymbol{F}_e^{T-1}$ and $\boldsymbol{F}_e^{T}$ eliminate each other, and Eq. (2) reduces to the linear modified transformation work criterion:

$$W = b_3\sigma_3\varepsilon_{t3} + b_1(\sigma_1 + \sigma_2)\varepsilon_{t1} = A. \tag{3}$$

The equality is used to describe the combination of stresses at the limit of stability and calibrate material parameters. W reduces to the transformation work for $b_1 = b_3 = 1$. The consequence of Eq. (3) for cubic-to-tetragonal PT is that, with $\varepsilon_{t1} = \varepsilon_{t2}$, the stresses σ_1 and σ_2 contribute to the instability criterion via $\sigma_1 + \sigma_2$, as in Eq. (1). Comparing Eqs. (3) and (1) with $\varepsilon_{t1} = U_{t1} - 1 = 0.243$ and $\varepsilon_{t3} = U_{t3} - 1 = -0.514$ leads to $A(\theta)/b_3 = 5.094$ GPa and $b_3/b_1 = 1.141$.

When shear stresses τ_{ij} are applied, causing nonzero deformation gradients F_{21}, F_{31}, and F_{32}, with rigid-body rotations excluded by imposing a constraint $F_{12} = F_{13} = F_{23} = 0$, Eq. (2) reduces to

$$W = b_3\sigma_3\varepsilon_{t3} + b_1(\sigma_1+\sigma_2)\varepsilon_{t1} + \frac{b_1\varepsilon_{t1} - b_3\varepsilon_{t3}}{F_{11}^e F_{22}^e}[\tau_{32}F_{32}^e F_{11}^e + \tau_{31}(F_{31}^e F_{22}^e - F_{32}^e F_{21}^e)] = A, \tag{4}$$

where $(b_1\varepsilon_{t1} - b_3\varepsilon_{t3})/A = 0.143$ and the terms proportional to $\varepsilon_{t2} - \varepsilon_{t1}$ are eliminated. With transformation shears absent in a cubic-to-tetragonal PT, the shear transformation work is absent. The terms proportional to the shear stresses are due to geometric nonlinearity (finite strains); they do not contain any additional material parameters. Shear stresses change the geometry of the crystal, and this affects transformation work along the normal components of transformation strain.

For the obtained parameters, and because $F_{ii}^e > 0$ and $\tau_{ij}F_{ij}^e > 0$, when τ_{32} and F_{32}^e or τ_{31} and F_{31}^e are applied alone, the contribution of shear stresses to W is positive; i.e., they promote tetragonal instabilities. Shear stress τ_{21} (more exactly, elastic shear strain F_{21}^e) alone or with τ_{32} does not contribute to the instability condition; but τ_{21} contributes when two other stresses, τ_{31} and τ_{32}, are applied simultaneously, and, depending on signs of all shear stresses, τ_{21} may promote or suppress tetragonal instability.

Shear stress-strain curves and shear lattice instability.—typical shear-stress–deformation-gradient (τ_{31}–F_{31}) curves (Fig. S3 [27]), shear instability starts at the maximum shear stress. This instability does not lead to Si II but rather to possible amorphization or hexagonal diamond Si IV (which is beyond our present focus).

Under an initial (before shear) hydrostatic compression, the shear instability at an infinitesimal shear starts at 72 GPa, i.e., below the tetragonal mode of lattice instability. This may explain amorphization in nanocrystalline Si I under increasing pressure when Si II PT is kinetically suppressed [44]. Amorphization may be caused by virtual melting [45] after crossing the metastable continuation of the melting line, as the melting temperature for Si reduces with pressure.

Effect of shear stresses on tetragonal instability.—$\sigma_3 - E_3$ curves were obtained for different fixed shears, along the path in the ($F_1 = F_2$, F_3) plane corresponding to $\sigma_1 = \sigma_2$ before shear. The instability stress (Fig. S4) is determined as the local maximum of $|\sigma_3|$ (Fig. 2). While during shear $\sigma_1 \neq \sigma_2$, but their sum $\sigma_1 + \sigma_2$ practically does not change. That is why curves in Fig. S4 are given for the fixed values of $(\sigma_1 + \sigma_2)/2$.

Absolute and relative deviations between the actual instability stress σ_3 and σ_3^{an} based on the analytical prediction (4) are small (Figs. S5 and S6) and can be neglected. Thus, the tetragonal lattice instability under the action of all six components of the stress tensor is described by the critical value of the modified transformation work [Eq. (4)], which (a) is linear in normal stresses, depends on $\sigma_1 + \sigma_2$, and has only two adjustable coefficients (b_1 and b_3), (b) is independent of $\sigma_1 - \sigma_2$ and shear stress τ_{21} acting alone or with one more shear stress, and (c) contains a geometric nonlinear term describing the contribution of all shear stresses without any additional adjustable parameters.

In summary, we augmented standard $T - P$ diagrams with criteria for structural and electronic instabilities (PTs) under a general applied stress tensor, providing guidance for more accessible processing routes for new or known high-pressure phases with novel properties. Our comprehensive DFT study of the PT between semiconducting Si I and metallic Si II under general applied stresses investigated stress-strain curves, elastic lattice instabilities, and regions of metallization. Metallization occurs deeply in the region of stability of Si I and is not caused by Si I → Si II PT. Deformed Si I becomes metallic, and the effect of

nonhydrostatic stresses is very strong. The hydrostatic PT pressure is ~21 times larger than for uniaxial loading. Such a strong nonhydrostatic stress effect at least partially explains the significant difference between the observed PT pressure (9–12 GPa) and the instability pressure of 75.81 GPa and the scatter in measured data under quasihydrostatic conditions.

Our key result is that Si I → Si II PT is given by a critical value of the modified transformation work [Eq. (4)]. For a general stress tensor (six independent variables), the PT criterion has just two parameters. Hence, PT criterion can be determined by just two DFT calculations versus applied stress.

These results are significant for creating new, more practical, and economical processing routes for discovery and stabilizing materials with novel properties. While comparison of the Gibbs free energy minima defines thermodynamic equilibrium (possibly unachievable in practice), we suggest the competition of instabilities to serve for phase selection. Critically, this approach enables ways to reduce PT pressure due to nonhydrostatic stresses by an order of magnitude or more [5,13–15]. They can also be used for quantitative studies of the influence of crystal defects on phase transitions [17,18] and quantitatively rationalize connections between PT conditions for ideal and real (defective) crystals.

N. A. Z. and D. D. J. are supported by the U.S. Department of Energy (DOE), Office of Science, Basic Energy Sciences, Materials Science and Engineering Division. N. A. Z. completed this work with support by DOE's Advanced Manufacturing Office, Office of Energy Efficiency and Renewable Energy, through CaloriCool™. Ames Laboratory is operated for DOE by Iowa State University under Contract No. DE-AC02-07CH11358. V. I. L. and H. C. are supported from NSF (CMMI-1536925 and DMR-1434613), ARO (W911NF-17-1-0225), ONR (N00014-16-1-2079), and Extreme Science and Engineering Discovery Environment (XSEDE) (TG-MSS140033 and MSS170015).

*zarkev@ameslab.gov
†haochen@iastate.edu
‡vlevitas@iastate.edu
§ddj@iastate.edu,ddj@ameslab.gov

[1] E. Y. Tonkov and E. Ponyatovsky, *Phase Transformations of Elements under High Pressure* (CRC Press, Boca Raton, 2004), Vol. 4.
[2] N. A. Zarkevich and D. D. Johnson, Coexistence pressure for a martensitic transformation from theory and experiment: Revisiting the bcc-hcp transition of iron under pressure, Phys. Rev. B **91**, 174104 (2015).
[3] T. Schindler and Y. K. Vohra, A micro-Raman investigation of high-pressure quenched graphite, J. Phys. Condens. Matter **7**, L637 (1995).
[4] V. L. Solozhenko, Boron nitride phase diagram. State of the art, High Press. Res. **13**, 199 (1995).
[5] C. Ji, V. I. Levitas, H. Zhu, J. Chaudhuri, A. Marathe, and Y. Ma, Shear-induced phase transition of nanocrystalline hexagonal boron nitride to wurtzitic structure at room temperature and lower pressure, Proc. Natl. Acad. Sci. U.S.A. **109**, 19108 (2012).
[6] R. Hill and F. Milstein, Principles of stability analysis of ideal crystals, Phys. Rev. B **15**, 3087 (1977).
[7] F. Milstein, J. Marschall, and H. E. Fang, Theoretical bcc-fcc Transitions in Metals via Bifurcations under Uniaxial Load, Phys. Rev. Lett. **74**, 2977 (1995).
[8] J. Wang, S. Yip, S. R. Phillpot, and D. Wolf, Crystal Instabilities at Finite Strain, Phys. Rev. Lett. **71**, 4182 (1993).
[9] G. Grimvall, B. Magyari-Köpe, V. Ozoliņš, and K. A. Persson, Lattice instabilities in metallic elements, Rev. Mod. Phys. **84**, 945 (2012).
[10] J. Pokluda, M. Černý, M. Šob, and Y. Umeno, Ab initio calculations of mechanical properties: Methods and applications, Prog. Mater. Sci. **73**, 127 (2015).
[11] V. I. Levitas, H. Chen, and L. Xiong, Lattice instability during phase transformations under multiaxial stress: Modified transformation work criterion, Phys. Rev. B **96**, 054118 (2017).
[12] V. I. Levitas, H. Chen, and L. Xiong, Triaxial-Stress-Induced Homogeneous Hysteresis-Free First-Order Phase Transformations with Stable Intermediate Phases, Phys. Rev. Lett. **118**, 025701 (2017).
[13] V. I. Levitas, High-pressure mechanochemistry: Conceptual multiscale theory and interpretation of experiments, Phys. Rev. B **70**, 184118 (2004).
[14] V. D. Blank and E. I. Estrin, *Phase Transitions in Solids under High Pressure* (CRC Press, Boca Raton, 2013).
[15] K. Edalati and Z. Horita, A review on high-pressure torsion (HPT) from 1935 to 1988, Mater. Sci. Eng. A **652**, 325 (2016).
[16] V. I. Levitas, High pressure phase transformations revisited, J. Phys. Condens. Matter **30**, 163001 (2018).
[17] V. I. Levitas and M. Javanbakht, Phase transformations in nanograin materials under high pressure and plastic shear: Nanoscale mechanisms, Nanoscale **6**, 162 (2014).
[18] M. Javanbakht and V. I. Levitas, Phase field simulations of plastic strain-induced phase transformations under high pressure and large shear, Phys. Rev. B **94**, 214104 (2016).
[19] N. A. Zarkevich, Structural database for reducing cost in materials design and complexity of multi-scale computations, Complexity **11**, 36 (2006).
[20] K. Mizushima, S. Yip, and E. Kaxiras, Ideal crystal stability and pressure-induced phase transition in silicon, Phys. Rev. B **50**, 14952 (1994).
[21] K. Gaál-Nagy, M. Schmitt, P. Pavone, and D. Strauch, Ab initio study of the high-pressure phase transition from the cubic-diamond to the beta-tin structure of Si, Comput. Mater. Sci. **22**, 49 (2001).
[22] Y. Umeno and M. Černý, Effect of normal stress on the ideal shear strength in covalent crystals, Phys. Rev. B **77**, 100101 (2008).

[23] M. Černý, P. Řehák, Y. Umeno, and J. Pokluda, Stability and strength of covalent crystals under uniaxial and triaxial loading from first principles, J. Phys. Condens. Matter **25**, 035401 (2013).
[24] R. Telyatnik, A. Osipov, and S. Kukushkin, Ab initio modelling of nonlinear elastoplastic properties of diamond-like C, SiC, Si, Ge crystals upon large strains, Mater. Phys. Mech. **29**, 1 (2016); http://www.ipme.ru/e-journals/MPM/no_12916/MPM129_01_telyatnik.html.
[25] V. I. Levitas, Phase-field theory for martensitic phase transformations at large strains, Int. J. Plast. **49**, 85 (2013).
[26] V. I. Levitas, Phase field approach for stress- and temperature-induced phase transformations that satisfies lattice instability conditions. Part I. General theory, Int. J. Plast. **106**, 164 (2018).
[27] See Supplemental Material at http://link.aps.org/supplemental/10.1103/PhysRevLett.121.165701 for simulation methods, a comparison of results with DFT and Tersoff potentials, the electronic band gap under loading, shear lattice instability, the effect of shear on tetragonal instability, and Refs. [28–38], as well as the data sets for all figures [39].
[28] G. Kresse and J. Hafner, Ab initio molecular dynamics for liquid metals, Phys. Rev. B **47**, 558 (1993).
[29] G. Kresse and J. Hafner, Ab initio molecular-dynamics simulation of the liquid-metal - amorphous-semiconductor transition in germanium, Phys. Rev. B **49**, 14251 (1994).
[30] G. Kresse and J. Furthmüller, Efficiency of ab-initio total energy calculations for metals and semiconductors using a plane-wave basis set, Comput. Mater. Sci. **6**, 15 (1996).
[31] P. E. Blöchl, Projector augmented-wave method, Phys. Rev. B **50**, 17953 (1994).
[32] G. Kresse and D. Joubert, From ultrasoft pseudopotentials to the projector augmented-wave method, Phys. Rev. B **59**, 1758 (1999).
[33] J. P. Perdew, K. Burke, and M. Ernzerhof, Generalized Gradient Approximation Made Simple, Phys. Rev. Lett. **77**, 3865 (1996).
[34] N. A. Zarkevich and D. D. Johnson, Nudged-elastic band method with two climbing images: Finding transition states in complex energy landscapes, J. Chem. Phys. **142**, 024106 (2015).
[35] H. J. Monkhorst and J. D. Pack, Special points for Brillouin-zone integrations, Phys. Rev. B **13**, 5188 (1976).
[36] D. D. Johnson, Modified Broyden's method for accelerating convergence in self-consistent calculations, Phys. Rev. B **38**, 12807 (1988).
[37] H. Balamane, T. Halicioglu, and W. Tiller, Comparative study of silicon empirical interatomic potentials, Phys. Rev. B **46**, 2250 (1992).
[38] P. Güttinger, Das Verhalten von Atomen im magnetischen Drehfeld, Z. Phys. **73**, 169 (1932).
[39] Supporting data is available at https://doi.org/10.25380/iastate.7125368.
[40] W. Yim and R. Paff, Thermal expansion of AlN, sapphire, and silicon, J. Appl. Phys. **45**, 1456 (1974).
[41] K. Gaál-Nagy and D. Strauch, Phonons in the β-tin, Imma, and sh phases of silicon from ab initio calculation, Phys. Rev. B **73**, 014117 (2006).
[42] N. A. Zarkevich, V. I. Levitas, H. Chen, and D. D. Johnson (to be published).
[43] N. A. Zarkevich and D. D. Johnson, Magneto-structural transformations via a solid-state nudged elastic band method: Application to iron under pressure, J. Chem. Phys. **143**, 064707 (2015).
[44] S. K. Deb, M. Wilding, M. Somayazulu, and P. F. McMillan, Pressure-induced amorphization and an amorphous–amorphous transition in densified porous silicon, Nature (London) **414**, 528 (2001).
[45] V. I. Levitas, Crystal-Amorphous and Crystal-Crystal Phase Transformations via Virtual Melting, Phys. Rev. Lett. **95**, 075701 (2005).